Available online at www.sciencedirect.com
SCIENCE DIRECT®
Journal of Solid State Chemistry 173 (2003) 209–215
JOURNAL OF SOLID STATE CHEMISTRY
http://elsevier.com/locate/jssc

Evolution and characterization of fluorite-like nano-$SrBi_2Nb_2O_9$ phase in the $SrO–Bi_2O_3–Nb_2O_5–Li_2B_4O_7$ glass system

N. Syam Prasad,[a] K.B.R. Varma,[a,*] Y. Takahashi,[b] Y. Benino,[b] T. Fujiwara,[b] and T. Komatsu[b]

[a] *Materials Research Centre, Indian Institute of Science, Bangalore 560 012, India*
[b] *Department of Chemistry, Nagaoka University of Technology, Nagaoka 940-2188, Japan*

Received 31 August 2002; received in revised form 2 December 2002; accepted 11 December 2002

Abstract

Transparent glasses of various compositions in the system $(100-x)Li_2B_4O_7–x(SrO–Bi_2O_3–Nb_2O_5)$ (where $x = 10$, 20, 30, 40, 50 and 60, in molar ratio) were fabricated via splat quenching technique. The glassy nature of the as-quenched samples was established by differential thermal analyses. X-ray powder diffraction (XRD) and transmission electron microscopic studies confirmed the amorphous nature of the as-quenched and crystallinity in the heat-treated samples. Fluorite phase formation prior to the perovskite $SrBi_2Nb_2O_9$ phase was analyzed by both the XRD and high-resolution transmission electron microscopy. Dielectric and the optical properties (transmission, optical band gap and Urbach energy) of these samples have been found to be compositional dependent. Refractive index was measured and compared with the values predicted by Wemple–Didomemenico and Gladstone–Dale relations. The glass nanocomposites comprising nanometer-sized crystallites of fluorite phase were found to be nonlinear optic active.

Keywords: Glassnanocomposites; $SrBi_2Nb_2O_9$; Fluoride like phase; Second harmonic generation; Ferroelectric; Dielectric

1. Introduction

In recent years, there has been a considerable interest in the ferroelectric Aurivillius layered oxides, because of their potential use in ferroelectric random access memories [1–3]. In comparison with nonlayered perovskite ferroelectrics such as $Pb(Zr,Ti)O_3$ (PZT), these offer several advantages such as fatigue-free, lead-free and low operating voltages [4,5]. $SrBi_2Nb_2O_9$ (SBN) which is an $n = 2$ member of the same family is proved to be versatile for ferroelectric and other related properties. Recently, SBN thin films were well characterized for possible applications in the memory devices [6,7]. However, the optical properties, recognized to be important from the optical device point of view, were not fully investigated. For this purpose, one should have optical-quality bulk single crystals with the desired dimensions. Unfortunately, the single-crystal growth of SBN was hampered because of its high melting point, dissociation characteristics and the bismuth loss (high volatility) encountered in the process. Therefore, we have been exploring alternative ways of obtaining transparent materials via glass–ceramic route. Since constituent oxides of SBN do not possess ready glass-forming capability on their own, when they are subjected to conventional quenching techniques, we thought it is worth investigating into polar and optical properties of in situ grown SBN phase in $Li_2B_4O_7$ (LBO) glass matrix, though there is a mismatch in the refractive indices.

Recently, we reported the SBN perovskite phase formation in the system $(100-x)Li_2B_4O_7–x(SrO–Bi_2O_3–Nb_2O_5)$ (x ranging from 10 to 60, in molar ratio) via fluorite phase formation [8]. Many reports are available in the literature related to the fluorite formation prior to the perovskite phase on the other ferroelectric oxides [9–11]. Though there exist some data on SBN fluorite phase, it is not fully characterized for its physical properties. In this paper, we report the results concerning the glass formation and evolution of the nanocrystalline SBN fluorite-like phase in the glass

*Corresponding author. Fax: +91-80-360-0683.
E-mail address: kbrvarma@mrc.iisc.ernet.in (K.B.R. Varma).

0022-4596/03/$ - see front matter © 2003 Published by Elsevier Science (USA).
doi:10.1016/S0022-4596(03)00026-4

system. Dielectric, linear and nonlinear optical (NLO) characteristics are also elucidated in this paper.

2. Experimental

Transparent glasses in the composition $(100-x)Li_2B_4O_7-x(SrO-Bi_2O_3-Nb_2O_5)$ (where $x = 10$, 20, 30, 40, 50 and 60, in molar ratio) were fabricated by melting the mixtures of reagent grade $SrCO_3$, Bi_2O_3, Nb_2O_5 and pre-reacted LBO. Well-mixed batches were melted in a platinum crucible at 1100°C for 1 h to yield 15 g of the glass. Melts were quenched by pouring onto a stainless-steel plate that was maintained at 150°C and pressed with another plate to obtain 1–1.5 mm thick glass plates. These samples were heat-treated at 325°C (well below the glass transition temperature) for 6 h to anneal out the thermal stresses that are likely to exist. The photographs of the as-quenched and 500°C heat-treated samples of different compositions are illustrated in Fig. 1.

The as-quenched and heat-treated samples at different temperatures (500°C and 550°C for 6 h) were subjected to X-ray powder diffraction (XRD) studies using Cu$K\alpha$ radiation (SCINTAG, USA) to assess the amorphous and crystalline nature of the as-quenched and heat-treated samples, respectively. The glassy nature of the as-quenched samples was established by subjecting them to differential thermal analyses (DTA) (Polymer Laboratories STA 1500) in the 30–1000°C temperature range. A uniform heating rate of 15°C/min was adopted for this purpose. Three samples of each composition were subjected to DTA and the average value of the glass transition (T_g) and crystallization temperatures (T_{cr}) was determined. JEOL JEM 200CX transmission electron microscope (TEM) was employed for electron diffraction and high-resolution transmission electron microscopic (HRTEM) studies on the as-quenched and heat-treated samples.

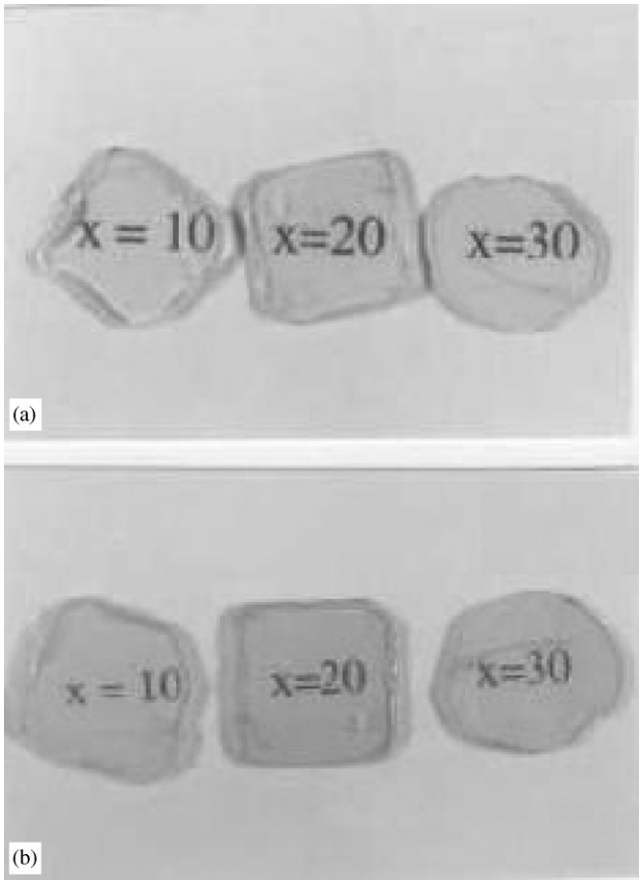

Fig. 1. Photographs of the (a) as-quenched and (b) heat-treated (at 500°C/6 h) glasses.

The capacitance and the dielectric loss measurements on both the as-quenched and heat-treated (500°C/6 h) samples were done using an impedance gain phase analyzer (HP 4194 A) in the frequency range 100 Hz–10 MHz with a signal strength of 0.5 V rms. For this purpose, polished plates were gold electroded and thin copper leads were bonded using the silver epoxy. The ferroelectric hysteresis loop (P vs. E) was photographed at a switching frequency of 50 Hz using an indigenously built modified Sawyer–Tower circuit.

The optical transmission spectra of the polished as-quenched and heat-treated samples (glass nanocomposites—GNC) were recorded in the wavelength range of 200–900 nm, using a Hitachi U3000 spectrophotometer. Refractive indices of the glasses and those heat-treated at 500°C were determined by Brewster's angle method at 570 nm. The second-harmonic intensity of the heat-treated glasses was measured by using a fundamental wave of Q-switched Nd^{+3}: YAG laser at a wavelength of $\lambda = 1064$ nm as a function of the angle of the incident light (the Maker fringe method). The second-harmonic intensity was observed in p-excitation and p-detection mode.

3. Results and discussion

DTA runs were made to determine the glass transition (T_g), crystallization (T_{cr}) and melting temperatures (T_m). The DTA curves that were obtained for the as-quenched glass pieces corresponding to the representative compositions $x = 20$, 30 and 40 are shown in Figs. 2a–c. We observe three exotherms (second exotherm is not that distinct in the case of $x = 20$) and an endotherm for all the as-quenched samples under study. The exotherms corresponding to the crystallization temperatures (T_{cr1}, T_{cr2} and T_{cr3}) were found to occur in the range 480–630°C. A subsequent endotherm that is encountered around 800°C is attributed to the melting of the glass composite (T_m). DTA traces that were obtained for the samples heat-treated at 500°C/6 h (just above the onset

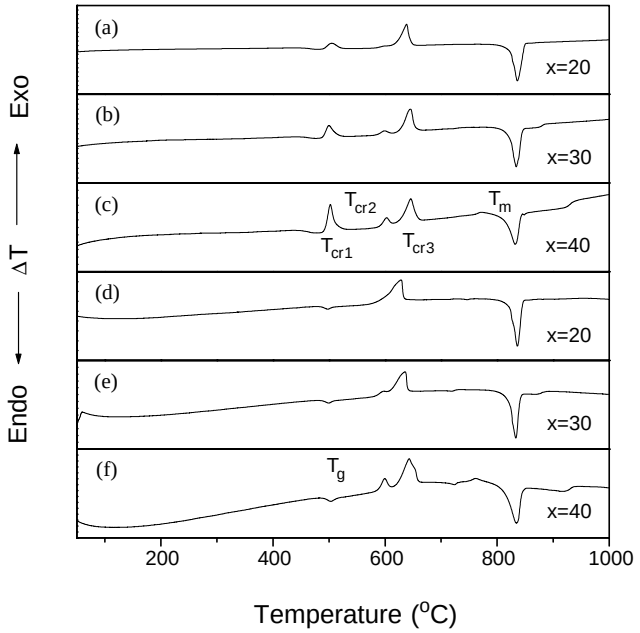

Fig. 2. Differential thermograms of the as-quenched (a)–(c) and 500°C heat-treated (d)–(f) glasses.

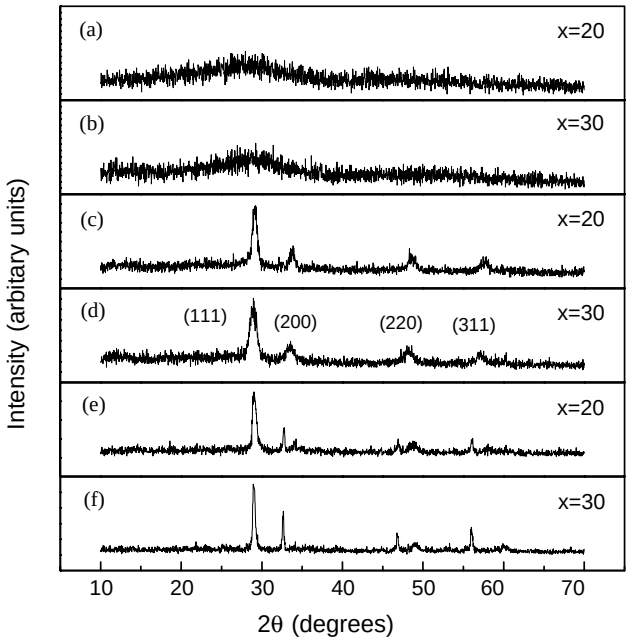

Fig. 3. XRD patterns for the as-quenched ((a) and (b)) and heat-treated ((c) and (d) are for 500°C; (e) and (f) are for 550°C) glasses of different compositions.

of the first exotherm) corresponding to the compositions $x = 20$, 30 and 40 are depicted in Figs. 2d–f. Interestingly, these show only last two exotherms (except in the case of $x = 20$) and a clear glass transition temperature (T_g) which was perhaps masked by the first exotherm in the as-quenched samples. XRD analyses have been carried out to investigate into the evolution of the phases that are associated with each exotherm.

Fig. 3 shows the X-ray diffraction patterns recorded for the as-quenched and heat-treated (at different temperatures) glasses in the composition $(100-x)Li_2B_4O_7-x(SrO-Bi_2O_3-Nb_2O_5)$ (where $x = 10$, 20, 30, 40, 50 and 60, in molar ratio). The broad XRD patterns obtained for the as-quenched glasses of the representative compositions $x = 20$ and 30 are shown in Figs. 3a and b. These results confirm their amorphous nature. The XRD patterns recorded for the samples ($x = 20$ and 30) heat-treated in the vicinity of first exotherm (500°C) are shown in Figs. 3c and d. The *d*-spacings that are calculated based on these patterns are found to correspond to the fluorite phase of SBN [8]. Upon further heating at 550°C/6 h (in the vicinity of the second exotherm), the fluorite phase has transformed to the perovskite SBN phase (Figs. 3e and f, respectively for $x = 20$ and 30). The lattice parameters ($a = 5.4946$ $b = 5.4979$ and $c = 25.1095$ Å) computed based on this pattern are comparable with those reported ($a = 5.5189$ $b = 5.5154$ and $c = 25.1124$ Å) in the literature [12] for a typical polycrystalline distorted perovskite SBN phase. The samples that are heat-treated beyond the third exotherm exhibited XRD patterns corresponding to both SBN and LBO.

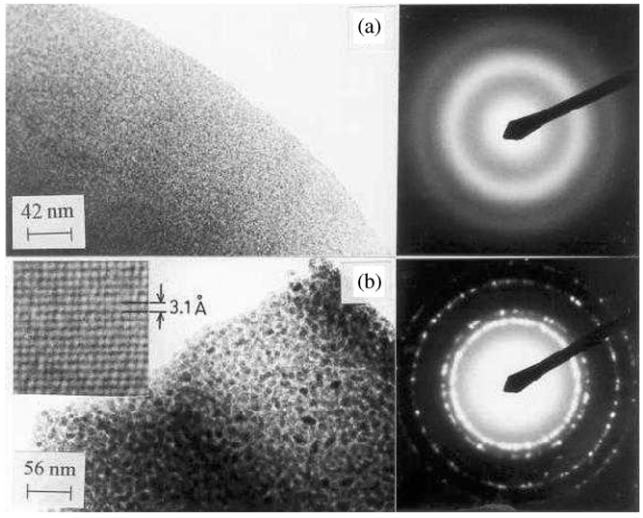

Fig. 4. Transmission electron micrographs along with the SAED patterns recorded for the (a) as-quenched and (b) 500°C heat-treated glasses. High-resolution lattice image is shown in the inset of (b).

Transmission electron micrographs along with the selected area electron diffraction (SAED) patterns recorded for the as-quenched and heat-treated (500°C) samples of the representative composition $x = 50$ are shown in Fig. 4. The diffraction pattern (Fig. 4a) that was obtained for the as-quenched glass indicates its overall amorphous nature. The incidence of nearly sharp spherical rings around the bright central region suggests the presence of local ordered regions. Further, it is confirmed that the area of the ordered regions increases

with increase in the composition x. Fig. 4b shows a bright field image obtained for the sample heat-treated at 500°C which indicates a fine distribution of spherical crystallites in the LBO glass matrix. The average crystallite size is found to lie in the range 12–20 nm depending on the composition x ranging from 20 to 60. The d-spacings obtained based on the electron diffraction pattern are 3.078, 2.674, 1.895, 1.614 and 1.55 Å. These d-spacings obtained from the SAED pattern are in close agreement with that of the reported values for the fluorite (CaF_2) phase [13]. HRTEM of these crystallites reveal a lattice spacing of 3.1 Å (inset of Fig. 4b). This corresponds to the (111) lattice spacing of the fluorite structure.

The dielectric constant (ε_r) and the dielectric loss (D) measurements were carried out on different compositions in the system $(100-x)Li_2B_4O_7-x(SrO–Bi_2O_3–Nb_2O_5)$ $(10 \leqslant x \leqslant 60)$ (in molar ratio). The dielectric constant and loss recorded at 100 kHz (25°C) for the GNC (glasses containing 12–20 nm sized crystallites of fluorite SBN) for all the compositions are listed in Table 1. The dielectric constant for the GNC increases with increase in SBN composition whereas the loss decreases (though the variation is small) systematically. The increase in the dielectric constant could be rationalized by the Clausius–Mossotti equation

$$\frac{\varepsilon_r - 1}{\varepsilon_r + 2} = \frac{4\pi N_A \alpha_s}{3}\frac{\rho}{M_g},$$

where ρ is the density, M_g is the molecular weight of the glass composition α_s is the static polarizability and N_A is the Avogadro's number. The static polarizabilities obtained from the above equation for GNC are listed in Table 1. Static polarizability (α_s) increases with increase in SBN content which is consistent with that of ε_r behavior.

The optical transmission spectra (uncorrected for reflection losses) were recorded at room temperature for all the as-quenched and heat-treated (at 500°C/6 h) samples in the wavelength range 200–900 nm. Fig. 5 shows the transmission spectra for both the GNC (heat-treated at 500°C/6 h) of the compositions $x = 20$ and 60.

Table 1
Compositional dependence of dielectric constant (ε_r), $\tan\delta$, static polarizability (α_s), $\lambda_{cut\text{-}off}$ and optical band gap energy (E_g) of the glasses heat-treated at 500°C/6 h

X	ε_r at 100 kHz	$\tan\delta$ at 100 kHz	α_s (10^{-24} cm^3)	$\lambda_{cut\text{-}off}$ (nm)	E_g (eV)
10	14	0.024	25.65	399	2.93
20	19	0.018	28.69	406	2.87
30	25	0.013	30.78	412	2.83
40	32	0.008	33.65	417	2.8
50	40	0.006	36.17	422	2.78
60	50	0.005	38.61	425	2.76

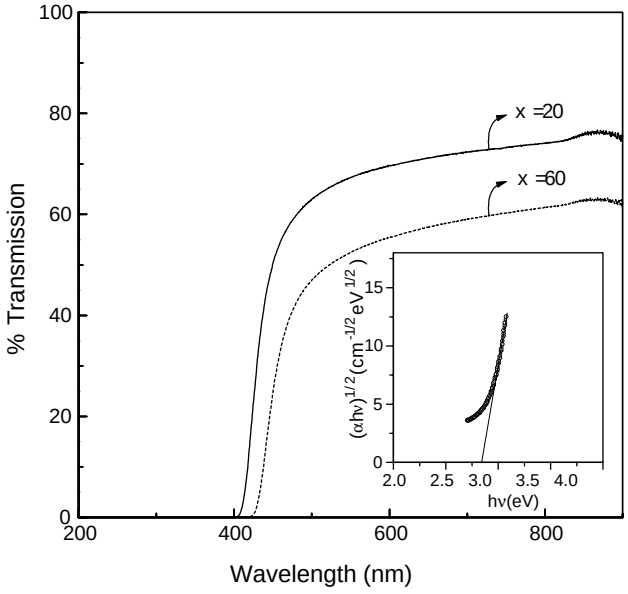

Fig. 5. Optical transmission spectra for the polished GNC samples. Inset shows the Taus plot for $x = 20$.

The percentage transmission from 900 to 500 nm is almost constant for all the samples. The transmission suddenly drops and reaches almost zero below 450 nm. The wavelength at which the percentage transmission is zero is referred to as $\lambda_{cut\text{-}off}$ This $\lambda_{cut\text{-}off}$ shifts towards longer wavelengths of the spectra as the SBN content increases (Table 1). The optical band gap (E_g) of all the glass compositions was calculated from the Tauc plot ($(\alpha h\nu)^{1/2}$ vs. $h\nu$) generated based on the transmission data. Typical Tauc plot for the GNC of composition $x = 20$ is shown in the inset of Fig. 5. The E_g decreases as the concentration of SBN increases (see Table 1) for the GNC samples under study. The width of band tails extended into the band gap, expressed in terms of Urbach energy obtained by plotting $\ln(\alpha)$ vs. $h\nu$ for the samples heat-treated at 500°C shown in Table 1. It is observed that the Urbach energy decreases from 165 to 90 meV as the content (x) of SBN increases. The decrease in the Urbach energy suggests the possibility of local long-range order arising from the decrease in the number of defects with increase in the SBN composition.

The compositional dependence of the refractive indices at 570 nm of the GNC obtained via Brewster's angle method is shown in Fig. 6. A notable increase in the refractive index with increase in the SBN composition x was found. Refractive index of oxide could be predicted by using various empirical relations. According to Wemple and Didomemenico [14] the refractive index is inversely related to the band gap E_g in electron volts

$$n^2 \cong 1 + \frac{15}{E_g}.$$

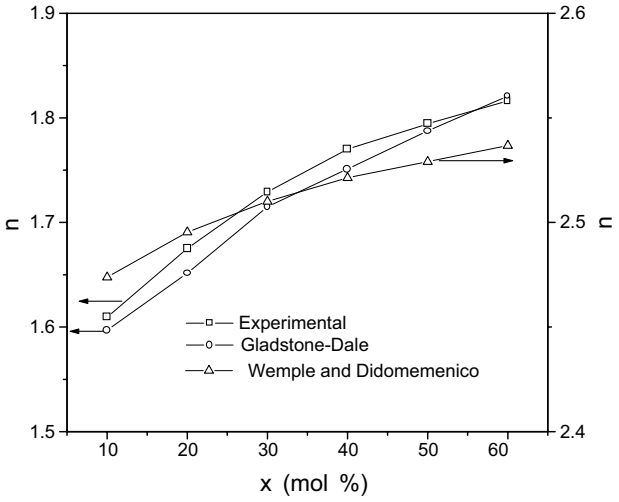

Fig. 6. Refractive index predicted and measured for GNC with variation of the SBN content.

Gladstone and Dale proposed another empirical relation [15] to predict the refractive indices

$$n = 1 + \rho \sum_i p_i k_i,$$

where ρ is density, and p_i and k_i are the weight fraction and refractive coefficient of the ith component. The refractive indices calculated using these relations are shown in Fig. 6. The refractive indices estimated by Gladstone–Dale relation are close to the experimental values of the present system. However, a small deviation observed from the experimental values can be attributed to the micro/nanostructure of the present composites. Also, the refractive index of any material is known to be wavelength dependent. Since, we do not have k_i values at the wavelength of the experimental data observed, a deviation of the kind encountered here is expected.

The optical polarizability (α_o) of the glass nanocomposites was calculated by using the Lorentz–Lorenz equation [16]

$$\alpha_o = \frac{3}{4\pi N_A}\frac{n^2-1}{n^2+2}V_m,$$

where n is the refractive index, N_A is the Avogadro's number or more strictly the number of polarizable ions per mole and V_m is the molar volume. Similarly, the molar refraction R_m is calculated using the equation

$$R_m = \frac{n^2-1}{n^2+2}V_m.$$

The variation of optical polarizability, molar refraction and molar volume of the GNC with variation in the SBN composition x is listed in Table 2. These are found to increase with increase in the composition x and consistent with the data on refractive indices.

The most important parameters dominating the linear optical response of condensed media is the polarization

Table 2
Compositional variation of density, molar volume, molar refraction and optical polarizability of the glasses heat-treated at 500°C/6 h

X	ρ (g/cm^3)	V_m (cm^3)	R_m (cm^3 mol^{-1})	α_o (10^{-24} cm^3)
10	2.96	79.7	27.6	10.94
20	3.58	84.5	31.7	12.58
30	4.22	87.4	34.9	13.81
40	4.68	93.1	38.7	15.34
50	5.11	98.3	41.8	16.56
60	5.50	103.4	44.9	17.78

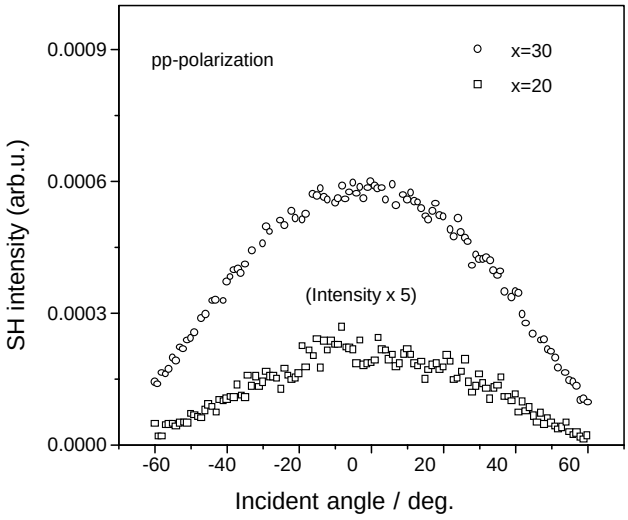

Fig. 7. Second-harmonic intensities for the GNC of two compositions as a function of the incident angle.

of the constituent atoms, ions and molecules. This is applicable to the third-order nonlinearity if there is a relation between the hyperpolarizability of a microscopic constituent and the linear polarizability. On the basis of the Johnson and Subbaswamy analysis [17], Adair and Wang derived the following relation [18,19] between α_o and χ^3:

$$\chi^3 = C'(n^2+2)^3(n^2-1)\alpha_o,$$

where C' is a constant, n refractive index, α_o is the linear polarizability and χ^3 is the third-order NLO susceptibility. The χ^3 estimated based on n and α_o is found to increase steadily with increase in the SBN composition x. The χ^3 values obtained for the present system are of the same order of magnitude reported for the La_2O_3–TeO_2 glass system [20]. Studies are in progress to measure χ^3 and evaluate C' for the present system based on the experimental data.

The transparent nature of the heat-treated glasses containing nanocrystalline fluorite phase of SBN, enabled us to measure the second-harmonic generation (SHG). The SH intensity as a function of the incident angle for the compositions $x = 20$ and 30 are shown in

Fig. 7. It is observed that the SH intensity increases with increase in the composition of SBN dispersed in the glassy LBO matrix. Even though there is no well-defined maker fringe pattern, the variation in SHG intensity with the angle of incidence is noteworthy. The detailed studies with regard to the calculation of the effective '*d*' coefficients and the influence of the crystallite size on the nature of the variation are in progress and will be communicated shortly.

The ferroelectric hysteresis loop studies have been carried out on the samples heat-treated at 500°C and 550°C, corresponding to the composition $x = 60$. Even though there are a few reports on the existence of the SBN fluorite phase, the data on its physical properties are scanty. In Fig. 8a, we show P vs. E measurements done on the samples heat-treated at 500°C. It is evident that the polarization varies linearly with the applied field. This clearly demonstrates that the cubic Sr–Bi–Nb oxide fluorite phase does not have any ferroelectric characteristics as reported by Hyun et al. [21]. However, the samples heat-treated at 550°C (comprising 0.3 μm sized crystallites of perovskite SBN) exhibited moderately good hysteresis loops in the temperature range 100–400°C confirming the ferroelectric nature of the heat-treated samples. Fig. 8b shows the P vs. E hysteresis loop photographed at 250°C. The values of P_r and E_c are 0.09 μC/cm^2 and 2.1 kV/cm, respectively. Ferroelectric loop recorded in the vicinity of the transition temperature (430°C) shows the near-linear behavior (not shown here) confirming the incidence of ferroelectric to paraelectric phase transition in these samples.

3.1. Fluorite phase formation

Metastable fluorite phase was encountered by many groups around the world when they attempted to prepare the ferroelectric phases from their respective oxides. Fluorite phase formation in the system PbO–ZrO_2–TiO_2 was reported when PZT was crystallized from its amorphous state [22]. Recently, there have been a few reports on the structures of SBN and SBT, when these were crystallized from their corresponding amorphous phases. SBT thin films, processed by soft chemistry route gave rise to fluorite phase at temperatures below 700°C. According to Rodriguez et al., SBT crystallizes in the fluorite form at lower temperatures and transforms to the required perovskite form at higher (>700°C) temperatures [23]. The fluorite phase of Bi_3NbO_7 was found to crystallize in the cubic system of space group $Fm\bar{3}m$ [24] similar to that of CaF_2.

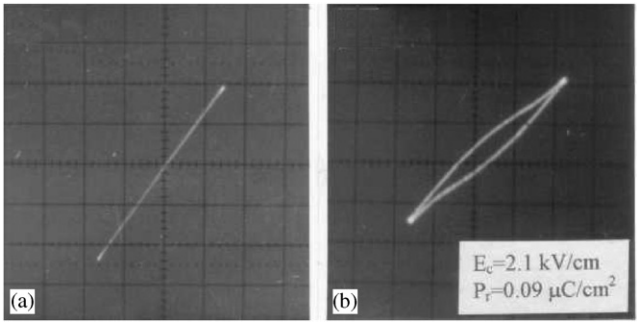

Fig. 8. P vs. E hysteresis loop recorded on the glass nanocomposite of the composition $x = 60$ heat-treated at two different temperatures (a) 500°C and (b) 550°C.

The fluorite phase of SBN was encountered when SBN powders were synthesized using aqueous solution method from mixtures of water-soluble compounds, Sr-EDTA, Bi-EDTA and Nb-citrate [25]. A number of issues emerge from the results of the present experiments and similar studies that were carried out by the earlier authors. This could be visualized in the following ways.

X-ray analysis on the fluorite phase of the title compound indicates a systematic shift in the peak positions towards higher angles with increase in the heat-treatment temperature (470–500°C). The unit-cell parameters, for a typical composition $x = 30$, that are calculated for the fluorite phase heat-treated at 470°C (5.382 Å) are found to be higher than those obtained for heat-treated at 500°C (5.349 Å) samples. This might be due to the progressive incorporation of niobium and strontium atoms originating from the amorphous matrix into δ-Bi_2O_3 as a host [26,27]. It is known that the high-temperature fluorite type δ-Bi_2O_3 phase could be stabilized at room temperature by doping with various cations [28,29]. This fact supports the formation of complex solid solution to start with, which is closely related to the host δ-Bi_2O_3 fluorite-like phase. Substitution of small Nb^{5+} and Sr^{2+} for the larger Bi^{3+} in the host δ-Bi_2O_3 phase gives rise to the lowering of lattice parameter in the samples heat-treated at higher temperatures [30] indicating the progressive incorporation of Nb^{5+} and Sr^{2+} at higher temperatures.

The cations in the perovskites are typically described as forming a bcc-type structure. Conversely, the cations in fluorite are in an fcc, wherein all positions are equivalent. The A^{2+} and B^{5+} cations in the perovskites are coordinated by 12 and 6 anions, respectively, whereas all cations (Sr^{2+}, Bi^{+3} and Nb^{5+}) in a fluorite with stoichiometry MO_2 (cation:anion ratio 1:2) would be coordinated by 8 anions. SBN which has the cation:anion ratio as 1:1.8 unlike in the typical case, would have strong tendency to form into defect fluorite structure in which all the cations could have the coordination number $\leqslant 8$ (8, 7 or 6). Indeed Castro in his study on the fluorite phase of Bi_3NbO_7 confirmed this fact [24].

It was reported in the literature [31] that the crystallization of perovskite under strong diffusional constraints would likely induce disorder in the form of

cation mixing between A and B sublattices. In the present case, Sr^{2+} could be accommodated at octahedral (B) site. Whereas the smaller cation Nb^{5+} occupying 12-fold coordination site would be less favorable. In contrast, all cation sites in the defect fluorite are equally coordinated and thus fluorite phase formation is kinetically favorable. Moreover, it is energetically favored over a hypothetical perovskite with complete disorder. In addition, the glass matrix involved in the present case eases the formation of fluorite by providing diffusional constraints in the form of glass.

Interestingly the nanocomposites, in which the SBN fluorite phase present in LBO glass matrix, under study are found to be NLO active. This is justified in the sense that local asymmetry/distortions within the overall transparent glass matrix is sufficient to give rise to nonlinearity unlike in the case of ferroelectric effects of cooperative nature. The incident laser beam which is confined to a small region (which is a general practice) of the sample (in the present case SBN-LBO composite) which is distorted from the typical fluorite structure will induce SHG. Fluorite crystallites would be under tremendous strain when these are crystallized from the glass. We believe that these stresses caused by the glass matrix could induce local noncentrosymmetry in the present nanocomposites and give rise to the observed SHG signals. It is extremely difficult to establish this conjecture by the conventional XRD and electron microscopy. In fact, our current attempts to map the local acentric regions have not been very successful. However, our sincere attempts are in progress to investigate into the origin of the present behavior of the SBN fluorite phase.

4. Summary and conclusions

Layered perovskite SBN phase formation, in the glass system $(100-x)Li_2B_4O_7-x(SrO–Bi_2O_3–Nb_2O_5)$ (where $x = 10$, 20, 30, 40, 50 and 60) was confirmed to be via an intermediate fluorite formation. The tendency to fluorite-like phase formation and its relative stability over perovskite at lower temperatures was briefly discussed. Static and optical polarizabilities of these GNCs increase with increase in the SBN content. The refractive indices predicted using Gladstone–Dale relation are found to be close to that of the experimental values. The optical transmission characteristics and the optical band gap of the title composite can be tuned depending on the extent of SBN composition. Most important aspect of this study is that these GNCs comprising SBN nanocrystallites of fluorite-like phase exhibit SHG.

Acknowledgments

The authors thank the Council of Scientific and Industrial Research (CSIR), Government of India for financial grant. One of the authors (Syam Prasad) acknowledges the University Grants Commission (UGC), Government of India, for a research fellowship. Also, the authors are grateful to Mr. Upadhyaya for his help in refractive index measurement.

References

[1] B. Aurivillius, Ark. Kemi. 1 (1951) 449.
[2] J.F. Scott, C.A.P. De Araujo, Science 246 (1989) 1400.
[3] S.B. Desu, D.P. Vijay, Mater. Sci. Eng. B 32 (1995) 75.
[4] C.A.P. De Araujo, J.D. Cuchlaro, L.D. Mc Millan, M.C. Scott, J.F. Scott, Nature 374 (1995) 627.
[5] T. Mihira, H. Yoshimori, H. Watanabe, C.A.P. De Araujo, Jpn. J. Appl. Phys. 34 (1995) 5233.
[6] Y. Cheol-Hoon, P. Sang-Shik, Y. Soon-Gil, Int. Ferroelectrics 21 (1998) 475.
[7] K. Amanuma, T. Hase, Y. Miyasaka, Appl. Phys. Lett. 66 (1995) 221.
[8] N. Syam Prasad, K.B.R. Varma, Mater. Sci. Eng. B 90 (2002) 246.
[9] T. Osaka, A. Sakakibara, T. Seki, S. Ono, I. Koiwa, A. Hashimoto, Jpn. J. Appl. Phys. 37 (1998) 597.
[10] J.G. Lisoni, P. Millan, E. Vila, J.L. Martin de Vidales, T. Hoffmann, A. Castro, Chem. Mater. 13 (2001) 2084.
[11] A. Seifert, F.F. Lange, J.S. Speck, J. Mater. Res. 10 (1995) 680.
[12] Ismunandar, B.J. Kennedy, J. Solid. State. Chem. 126 (1996) 135.
[13] JCPDS-International Center for Diffraction Data, 35-0816.
[14] S. Wemple, D. Didomenico, J. Appl. Phys. 40 (1969) 735.
[15] R.E. Newnham, Structure Property Relations, Springer, New York, 1975.
[16] M.B. Volf, Glass Science and Technology, Vol. 7, Elsevier, Amsterdam, 1984.
[17] M. Johnson, K. Subbaswamy, Phys. Rev. B 36 (1987) 9202.
[18] R. Adair, L.L. Chase, S.A. Payne, Phys. Rev. B 39 (1989) 3337.
[19] C. Wang, Phys. Rev. B 2 (1970) 2045.
[20] S-H. Kim, T. Yoko, S. Sakka, J. Am. Ceram. Soc. 76 (1993) 865.
[21] S.J. Hyun, B.H. Park, S.D. Bu, J.H. Jung, T.W. Noh, Appl. Phys. Lett. 73 (1998) 2518.
[22] A.P. Wilkinson, J.S. Speck, A.K. Cheetham, S. Natarajan, J.M. Thomas, Chem. Mater. 6 (1994) 750.
[23] M.A. Rodriguez, T.J. Boyle, C.D. Buchheit, R.G. Tissot, C.A. Drewien, B.A. Hernandez, M.O. Eatough, Int. Ferroelectrics 14 (1997) 201.
[24] A. Castro, E. Aguado, J.M. Rojo, P. Herrero, R. Enjalbert, J. Galy, Mater. Res. Bull. 33 (1998) 31.
[25] T. Asai, E.R. Camargo, M. Kakihana, M. Osada, J. Alloys Compounds 309 (2000) 113.
[26] C.D. Ling, R.L. Withers, S. Schmid, J.G. Thompson, J. Solid State Chem. 137 (1998) 42.
[27] W. Jhou, J. Solid State Chem. 163 (2002) 479.
[28] T. Takahashi, H. Iwahara, Mater. Res. Bull. 13 (1978) 1447.
[29] E.C. Subbarao, H.S. Maiti, Solid State Ion. 11 (1984) 317.
[30] A. Castro, D. Palem, J. Mater, Chem. 12 (2002) 2774.
[31] A.D. Polli, F.F. Lange, C.G. Levi, J. Am. Ceram. Soc. 83 (2000) 873.